

DESY 00-039
 MZ-TH/00-06
 TTP00-02
 hep-ph/0003082
 March 2000

ISSN 0418-9833

Photon Plus Jet Cross Sections in Deep Inelastic ep Collisions at Order $O(\alpha^2\alpha_s)$

A. Gehrmann-De Ridder¹, G. Kramer² and H. Spiesberger³

¹ Institut für Theoretische Teilchenphysik, Universität Karlsruhe,
 D-76128 Karlsruhe, Germany

² II. Institut für Theoretische Physik*, Universität Hamburg,
 Luruper Chaussee 149, D-22761 Hamburg, Germany

³ Institut für Physik, Johannes-Gutenberg-Universität,
 Staudinger Weg 7, D-55099 Mainz, Germany

e-mail: gehra@particle.physik.uni-karlsruhe.de,
 kramer@mail.desy.de, hspiesb@thep.physik.uni-mainz.de

Abstract

The production of a hard and isolated photon accompanied by one or two jets in large- Q^2 deep inelastic ep scattering is calculated at next-to-leading order. We include consistently contributions from quark-to-photon fragmentation and study various differential cross sections and their dependence on isolation cut parameters. Numerical results relevant for HERA experiments are presented.

*Supported by Bundesministerium für Bildung und Forschung, Bonn, Germany, under Contract 05 HT9GUA 3, and by EU Fourth Framework Program *Training and Mobility of Researchers* through Network *Quantum Chromodynamics and Deep Structure of Elementary Particles* under Contract ERB FMRX-CT98-0194.

1 Introduction

In the past, measurements of prompt photon production at both fixed-target facilities and hadron-hadron colliders, have extensively been used to constrain the gluon distribution of the proton [1]. Only recently the first data on prompt photon production in high-energy ep collisions have been reported [2]. Due to the presently still limited statistics the measurements are confined to prompt photons produced in photoproduction reactions, i.e. to ep collisions with almost real exchanged photons ($Q^2 \simeq 0$). As is well-known, photoproduction processes at high energies proceed by two distinct mechanisms. The incoming photon can couple either in a point-like manner to the incoming quark or antiquark (direct process) or hadronically as a source of quarks and gluons which in turn take part in the subsequent hard scattering process (resolved process). Therefore an important advantage of photoproduction measurements is to provide additional constraints on the quark and gluon content of the photon as suggested many years ago by Aurenche et al. [3].

By contrast, prompt photon production in deep inelastic scattering with large Q^2 , $Q^2 \gtrsim 10$ GeV², is fully determined by the direct process and does not need any non-perturbative input for the parton content of the photon¹ as in photoproduction. Therefore this process is sensitive only to the parton distribution functions (PDF's) of the proton. The possible information on the proton PDF's would be complementary to the F_2 measurement from inclusive deep inelastic scattering, since *up*- and *down*-type quarks contribute with different weights. Of course, the cross sections for $ep \rightarrow e\gamma X$ at large Q^2 are smaller than the corresponding cross sections for almost real photons; but with the larger luminosities planned at HERA rather accurate measurements of various differential cross sections for $Q^2 > 10$ GeV² seem feasible.

In addition to the perturbative direct production, photons are also produced through the “fragmentation” of a hadronic jet into a single photon carrying a large fraction of the jet energy [4]. This long-distance process is described in terms of the quark-to-photon and gluon-to-photon fragmentation functions (FF's).

In order to unambiguously identify the prompt photon signal from the hadronic background it is necessary to apply isolation cuts in the experiment. This has the effect of reducing the cross section due to a suppression of the photon fragmentation contributions. On the other hand, it has the advantage of eliminating to a large extent the dependence on the photon fragmentation function, which is a non-perturbative input and must come from other experiments designed to measure them.

To obtain reliable predictions it is necessary to calculate the $ep \rightarrow e\gamma X$ cross section in next-to-leading order (NLO) of the strong coupling constant α_s as has been done for $p\bar{p}$ collisions [5], e^+e^- annihilation [6, 7, 8], as well as photoproduction [9]. The corresponding NLO calculation of cross sections for prompt photon production in ep scattering with large Q^2 has not yet been done previously, neither for the technically simpler case of inclusive

¹At intermediate $Q^2 < 10$ GeV² there might be a significant resolved contribution which depends on the quark and gluon distribution of the *virtual* photon.

cross sections, i.e. without any photon isolation cut, nor for the case with isolation cuts. Applicability of perturbative QCD requires that the scattering process is characterized by a large transverse momentum, provided either by the momentum transfer Q^2 or a large transverse momentum of the hadronic final state. We consider only the case where both Q^2 is large and the hadronic final state is characterized by a large p_T . One specific possibility is to consider the case where in addition to the photon also one or more jets are observed in the final state. The detection of an additional jet may also help to identify the prompt photon events in the actual experiment. In leading order (LO) the photon is produced by the Compton process $\gamma^* + q \rightarrow \gamma + q$, where γ^* is a photon of high virtuality emitted by the incoming electron. This partonic photon production process contributes to the $\gamma + (1 + 1)$ -jet final state in ep scattering (the proton remnant jet being counted as “+1” jet as usual). In NLO the final states are $\gamma + (1 + 1)$ - and $\gamma + (2 + 1)$ -jets.

The first NLO calculations for this case were done by two of us and D. Michelsen [10]. This calculation was restricted to the case of not too large Q^2 where it is possible to neglect the exchange of a Z boson. Moreover, in this previous work the fragmentation contribution was not taken into account. Therefore, photon-quark collinear singularities could not be absorbed into the fragmentation functions. Instead, these singularities had been removed by explicit parton-level cutoffs. As a consequence, the result depended strongly on these parton-photon cutoffs, in particular for subprocesses with an incoming gluon. These cutoffs are difficult to control experimentally, where hadrons combined into jets are observed and not the partons needed to define the cutoffs. In subsequent work [11] we included the fragmentation contribution thereby avoiding the need to use parton-level cutoffs. The isolation criteria, which limit the hadronic energy in the jet containing the photon, are thus physical, i.e. correspond to selection criteria in the experimental analysis. In a later paper [12] we studied the sum of the $\gamma + (1 + 1)$ -jet and $\gamma + (2 + 1)$ -jet cross sections as a function of the momentum fraction carried by a photon inside a jet. We observed that this special cross section is sensitive to the fragmentation contribution, in particular to the quark-to-photon FF.

In [11], only a few observables have been calculated, as for example distributions with respect to the transverse momentum, p_T , and the rapidity, η , of the photon or the most energetic jet for one particular choice of the photon isolation cut. In this paper we take up the topic of this earlier work. Besides several other observables which are of interest for analyzing upcoming experimental data from HERA we shall present results for p_T and η distributions already considered in [11] for different isolation cuts. We also study possible scale dependencies to estimate the reliability of our predictions. As in [11] we use the $\gamma^* p$ center-of-mass system to define the kinematic variables. For most of the cross section calculations a particular cone algorithm is applied to define the parton jets and to isolate the photon signal. For a few cases we shall also make use of the k_T cluster algorithm.

The plan of the paper is as follows. In section 2 a brief outline of the theoretical background to the cross section calculations as well as the technique of the calculation are given. The results for the various observables are presented and discussed in section 3. Section 4 contains a summary and some concluding remarks.

2 Subprocesses Through Next-to-Leading Order

2.1 Leading-Order Subprocesses

In leading order, the production of photons in deep inelastic electron scattering is described by the quark (antiquark) subprocess (see Fig. 1)

$$e(p_1) + q(p_3) \rightarrow e(p_2) + q(p_4) + \gamma(p_5) \quad (1)$$

where the particle momenta are given in parentheses. The momentum of the incoming quark is a fraction ξ of the proton momentum P , $p_3 = \xi P$. The proton remnant r has the momentum $p_r = (1 - \xi)P$. It hadronizes into the remnant jet so that the process (1) gives rise to $\gamma + (1 + 1)$ -jet final states. In the virtual photon-proton center-of-mass system the hard photon recoils against the hard jet back-to-back. In a leading-logarithmic calculation, the effects of higher-order processes show up only via the use of the scale-violating parton distributions of the proton. The PDF's are calculated using collinear kinematics so that the event structure is the same as given by the lowest-order subprocesses, which are of order $O(\alpha^2)$ ².

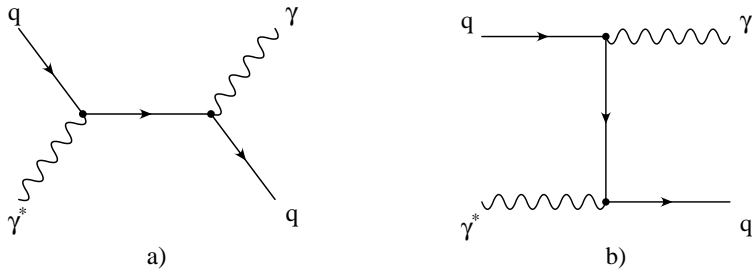


Figure 1: Feynman diagrams for $\gamma^* + q \rightarrow q + \gamma$.

To remove photon production by incoming photons with small virtuality and to restrict to the case where the scattered electron $e(p_2)$ is observed, one applies cuts on the usual deep inelastic scattering variables x , y , Q^2 as measured from the momentum of the scattered lepton. In particular we restrict the calculation to values of $Q^2 \geq 10$ GeV 2 ; however, since very large Q^2 values are not relevant at HERA we can neglect contributions from Z boson exchange. In addition, to have photons $\gamma(p_5)$ of sufficiently large energy we require an explicit cut on their transverse momentum. Finally, a cut on the invariant mass of the hadronic final state is also applied.

Both leptons and quarks emit photons. The subset of diagrams where the photon is emitted from the initial or final state lepton (leptonic radiation) is explicitly gauge invariant and can be considered separately. Similarly, the contribution from diagrams with a photon emitted from quark lines is called quarkonic radiation. In addition, there are also

²Here and in the following we do not count the extra factor α from the $ee\gamma^*$ vertex.

contributions from the interference of these two mechanisms. The emission of photons from leptons is described by pure QED and can be predicted with high reliability. Therefore, the contributions from leptonic radiation will be suppressed by cuts on the photon emission angle [10]. In our numerical evaluation we include the remaining background from leptonic radiation as well as the interference contribution.

At lowest order, each parton is identified with a jet and the photon is automatically isolated from the quark jet by requiring a non-zero transverse momentum of the photon or jet in the γ^*p center-of-mass frame. Therefore the photon fragmentation is absent in this order.

2.2 Subprocesses to Next-to-Leading Order

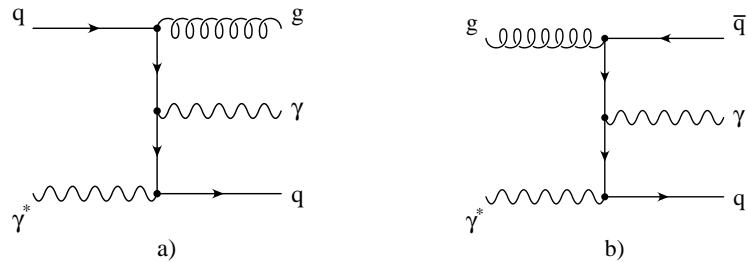


Figure 2: Examples of Feynman diagrams for higher-order processes: a) $\gamma^* + q \rightarrow q + g + \gamma$, b) $\gamma^* + g \rightarrow q + \bar{q} + \gamma$.

At next-to-leading order, processes with an additional gluon, either emitted into the final state or as incoming parton, have to be taken into account:

$$e(p_1) + q(p_3) \rightarrow e(p_2) + q(p_4) + \gamma(p_5) + g(p_6), \quad (2)$$

$$e(p_1) + g(p_3) \rightarrow e(p_2) + q(p_4) + \gamma(p_5) + \bar{q}(p_6), \quad (3)$$

where the momenta of the particles are again given in parentheses. Examples of diagrams for $\gamma^*q \rightarrow q\gamma g$ and $\gamma^*g \rightarrow q\gamma\bar{q}$ are shown in Fig. 2. In addition, virtual corrections (one-loop diagrams at $O(\alpha_s)$) to the LO processes (1) have to be included. The complete matrix elements for the processes (2) and (3) are given in [13]. The processes (2) and (3) contribute both to the $\gamma + (1+1)$ -jet cross section, as well as to the cross section for $\gamma + (2+1)$ -jets in the final state. In the latter case each parton in the final state builds a jet on its own, whereas for $\gamma + (1+1)$ -jets a pair of final state partons is experimentally unresolved. The criteria for combining two partons into one jet will be introduced later. The contributions (2) and (3) as well as the virtual corrections to (1) are of order $O(\alpha^2\alpha_s)$.

2.3 Fragmentation Contributions

In addition to the direct production described in the last two subsections, photons can also be produced through the fragmentation of a hadronic jet into a single photon carrying a large fraction of the jet energy [4]. This long-distance process is described in terms of quark-to-photon and gluon-to-photon fragmentation functions which absorb collinear singularities present in the NLO direct contributions of section 2.2. The corresponding fragmentation processes (see Fig. 3) are

$$e(p_1) + q(p_3) \rightarrow e(p_2) + q(p_4) + g(p_6), \quad (4)$$

$$e(p_1) + g(p_3) \rightarrow e(p_2) + q(p_4) + \bar{q}(p_6). \quad (5)$$

These processes are of order $\alpha\alpha_s$ whereas the photon FF is formally of order α , so that the LO fragmentation contribution is formally of order $O(\alpha^2\alpha_s)$, i.e. of the same order as the NLO direct contribution. The fragmentation photons, sometimes also called bremsstrahlung photons, are emitted predominantly along the direction of motion of the parent quark or gluon. Because of the pointlike nature of the photon-quark interaction, it is possible to calculate the leading-logarithmic behaviour of the photon FF, including the corrections due to additional gluon emissions. The resulting FF's are in fact of order $O(\alpha/\alpha_s)$ since they possess a logarithmic growth coming from the integration over the momenta of unobserved partons. Therefore in the leading-logarithmic approximation the fragmentation contribution is obtained from $O(\alpha/\alpha_s)$ FF's convoluted with corresponding $O(\alpha\alpha_s)$ cross sections for the two-body subprocesses (4) and (5). The resulting contribution is thus of order $O(\alpha^2)$, i.e. of the same order as the LO non-fragmentation process (1). For this reason it is sometimes argued that the fragmentation contribution should be combined with the LO direct process to provide the full LO physical cross section. Consequently, the calculation of the full cross section up to NLO would then also require the computation of the NLO corrections to the fragmentation contributions. On the other hand, it is well-known, that the fragmentation contribution in LO depends strongly on the factorization scale μ_F which, however, is cancelled to a large extent by the μ_F -dependence of the NLO contribution to the non-fragmentation part. For this reason and also since for

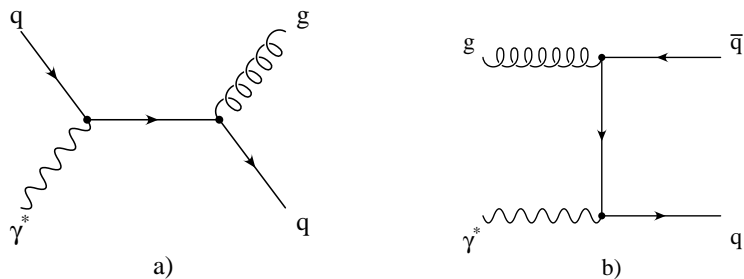


Figure 3: Feynman diagrams giving rise to fragmentation contributions: a) $\gamma^* + q \rightarrow q + g$, b) $\gamma^* + g \rightarrow q + \bar{q}$.

an isolated photon the fragmentation contribution is small we shall take it into account only in LO in the same way as in our previous work [11, 12].

The signature of the fragmentation contribution in LO is a photon balanced by a jet on the opposite side of the event and accompanied by nearly collinear hadrons on the same side of the event. This means that this contribution has a similar event structure as the LO direct contribution.

2.4 Calculational Details

The calculation of the NLO corrections was performed with the help of the phase space slicing method using a slicing parameter defined in terms of invariant masses. With this method it is straightforward to introduce the photon isolation requirement as well as to implement a jet definition which separates $\gamma + (1+1)$ -jet from $\gamma + (2+1)$ -jet final states. Phase space slicing based on invariant masses is also used to separate the photon-quark collinearly singular regions, however, using another independent cutoff parameter. The technical steps to apply the phase space slicing method in the present case are described in the following.

In the calculation of the contribution to the $\gamma + (1+1)$ -jet cross section we encounter the well-known infrared singularities. They appear in those phase space regions where two partons are degenerate to one parton, i.e. when the gluon becomes soft or two partons become collinear to each other. The singularities are assigned either to the initial state (ISR) or to the final state (FSR). Contributions involving the product of an ISR and a FSR factor are separated by partial fractioning. The FSR singularities cancel against singularities from virtual corrections to the LO process (1). For the ISR singularities, the cancellation is incomplete and the remaining singular contributions have to be factorized and absorbed into the renormalized PDF's of the proton.

To carry out these steps, the singularities are isolated in an analytic calculation using dimensional regularization. Since the corresponding calculations are too difficult for the exact cross sections of the processes (2) and (3) an approximate solution is required. To achieve this, the phase space slicing [14] is used first to separate the singular regions in the 4-particle phase space. Then, in these regions the matrix elements are approximated by their most singular contributions. Only for these approximate expressions and only in the singular regions the calculation is performed analytically. The separation of singular regions is obtained by applying a slicing cut y_0^J to the scaled invariant masses y_{ij} , where $y_{ij} = (p_i + p_j)^2/W_{\text{had}}^2$ and the mass of the hadronic final state W_{had} is defined by $W_{\text{had}}^2 = (P + q - p_5)^2$. The cut y_0^J must be chosen small enough so that terms of order $O(y_0^J)$ which are neglected in the singular approximation are so small that an accuracy of a few per cent is achievable for the final result. Outside the singular regions the integrations are done numerically without any approximation and with 4 space-time dimensions. Physical cross sections, as defined in the next section, are obtained by adding the contributions from singular and non-singular regions as well as the virtual contributions and subtracting the

remaining ISR collinear singularities. In the final results, the dependence on the slicing parameter y_0^J cancels. This means the cut-off y_0^J is purely technical. The independence on the slicing cut y_0^J has been checked by explicit calculation for some special photon plus jet cross sections in [10]. Further details and the derivation of the two-body matrix elements in the singular region together with the cancellation of the soft and collinear poles can be found in [13, 10].

In addition, the squared matrix elements for the processes (2) and (3) have photonic infrared and collinear singularities, i.e. singularities due to soft or collinear photons. Since we require the photon to be observed in the detector the infrared singularity can not occur. In the numerical analysis we will introduce this condition by requiring a minimum on the transverse momentum of the photon. This cut removes also all collinear singularities due to initial state radiation.

Final state collinear singularities due to photons are present and are treated again with the help of the phase space slicing method in a similar way as the quark-gluon collinear contributions. The phase space slicing parameter used to treat the photonic singularities can be chosen independently and is denoted by y_0^γ . As before, it has to be chosen very small so that the matrix element can be approximated by its singular part. For the subprocess (2), the phase space slicing is described by the squared invariant masses $y_{45} = (p_4 + p_5)^2/W_{\text{had}}^2$. In the gluon-initiated process (3) one has two singular regions which are controlled by the variables y_{45} and y_{56} , respectively. In the regions $y_{45}, y_{56} > y_0^\gamma$ the cross section is evaluated numerically in the same way as in [10] where these cuts were introduced as physical isolation cuts on the photon with sufficiently large isolation parameter y_0^γ . In this work the cuts on y_{45} and y_{56} are only technical since we include the contribution to the matrix element also in the regions $y_{45} < y_0^\gamma$ and $y_{56} < y_0^\gamma$. In these regions the matrix elements are collinearly divergent. The singularities are regulated by dimensional regularization, allowing us to absorb their divergent parts into the bare photon FF to yield the renormalized photon FF denoted by $D_{q \rightarrow \gamma}$. For the process (2) this procedure results in a contribution of the following form:

$$|M|_{\gamma^* q \rightarrow \gamma qg}^2 = |M|_{\gamma^* q \rightarrow qg}^2 \otimes D_{q \rightarrow \gamma}(z). \quad (6)$$

The matrix element $|M|^2$ on the right-hand side of (6) is the matrix element for the process $\gamma^* q \rightarrow qg$ whose Feynman diagram is shown in Fig. 3a. There exists a similar expression for the subprocess $\gamma^* g \rightarrow \gamma q\bar{q}$ (Fig. 3b). The photon FF $D_{q \rightarrow \gamma}(z)$ in (6) is given by [15, 8]

$$D_{q \rightarrow \gamma}(z) = D_{q \rightarrow \gamma}(z, \mu_F^2) + \frac{\alpha e_q^2}{2\pi} \left(P_{q\gamma}^{(0)}(z) \ln \frac{z(1-z)y_0^\gamma W^2}{\mu_F^2} + z \right). \quad (7)$$

$D_{q \rightarrow \gamma}(z, \mu_F^2)$ in (7) stands for the non-perturbative FF describing the transition $q \rightarrow \gamma$ at the factorization scale μ_F . This function will be specified in the next section. The second term in (7), if substituted in (6), is the finite part due to the collinear photon-quark (-antiquark) contribution to the matrix element $|M|_{\gamma^* q \rightarrow \gamma qg}^2$ integrated in the region $y_{45} < y_0^\gamma$ after absorption of the divergent part into the non-perturbative FF.

Again the parameter y_0^γ is only a parameter used in intermediate steps of the calculation, introduced to separate divergent from finite contributions; the y_0^γ -dependence in (7) is canceled by the dependence of the numerically computed $\gamma + (1+1)$ -jet cross section restricted to the region $y_{45} > y_0^\gamma$. Since the corresponding contributions to the matrix element in (6) are calculated in the collinear approximation, the result is valid only up to terms of order $O(y_0^\gamma)$. This requires to choose a very small value for y_0^γ . In Ref. [12] it has been explicitly shown that the sum of all terms for the photon plus jet cross section becomes independent of y_0^γ when y_0^γ is chosen small enough.

In (7), $P_{q\gamma}^{(0)}$ is the LO quark-to-photon splitting function

$$P_{q\gamma}^{(0)}(z) = \frac{1 + (1 - z)^2}{z} \quad (8)$$

and e_q is the electric charge of quark q . The variable z denotes the fraction of the quark momentum carried away by the photon. If the photon is emitted from the final state quark with 4-momentum $p'_4 = p_4 + p_5$, then z can be related to the invariants y_{35} and y_{34} :

$$z = \frac{y_{35}}{y_{34'}} = \frac{y_{35}}{y_{34} + y_{35}}. \quad (9)$$

The fragmentation contribution is proportional to the cross section for $\gamma^* q \rightarrow qg$ which is $O(\alpha\alpha_s)$ and is well-known. It must be convoluted with the function in (7) to obtain the contribution to the cross section for $\gamma^* q \rightarrow q\gamma g$ at $O(\alpha^2\alpha_s)$. Equivalent formulas are used to calculate the fragmentation contributions to the channel (3) and in the case where the quarks in the initial and final state are replaced by an antiquark in (2).

3 Results

3.1 Kinematical Selection Cuts and Other Input

The results for the cross sections which will be presented in the following subsections are obtained for energies and kinematical cuts appropriate for HERA experiments. The energies of the incoming electron (positron) and proton are $E_e = 27.5$ GeV and $E_P = 820$ GeV, respectively. The cuts on the DIS variables are chosen as in our previous works [11, 12]:

$$\begin{aligned} Q^2 &\geq 10 \text{ GeV}^2, & W_{\text{had}} &\geq 10 \text{ GeV}, \\ 10^{-4} &\leq x \leq 0.5, & 0.05 &\leq y \leq 0.95 \end{aligned} \quad (10)$$

where $Q^2 = -q^2$ and q is the electron momentum transfer, $q = p_1 - p_2$ as usual.

To reduce the background from leptonic radiation [10] we require

$$90^\circ \leq \theta_\gamma \leq 173^\circ, \quad \theta_{\gamma e} \geq 10^\circ \quad (11)$$

where θ_γ is the emission angle of the photon measured with respect to the momentum of the incoming electron in the HERA laboratory frame. The cut on $\theta_{\gamma e} (= \theta_{25})$, the angle between the momenta of the photon and the scattered electron, suppresses radiation from the final state electron. In the case of photon plus jet cross sections, the photon and the hadron jets J are required to have minimal transverse momenta in the $\gamma^* p$ center-of-mass system (i.e. in the rest system of $p_1 - p_2 + P$ where the remnant has $p_{T,r} = 0$),

$$p_{T,\gamma} \geq 5 \text{ GeV}, \quad p_{T,J} \geq 6 \text{ GeV}. \quad (12)$$

Note that an event is rejected if we do not find at least one jet with $p_{T,J}$ above the cut in (12). If there are two partons with $p_{T,J} \geq 6 \text{ GeV}$, the event has a chance to be treated as a $\gamma + (2+1)$ -jet event. If, after trying to recombine partons into jets (see below), only one jet has $p_{T,J} \geq 6 \text{ GeV}$, the event contributes to the $\gamma + (1+1)$ -jet class. In the latter case, it may happen that there is an additional parton not combined into a jet with $p_{T,i} < 6 \text{ GeV}$ (in a JADE-like jet algorithm applied in the HERA laboratory frame, such a low- p_T parton would be recombined with the remnant jet in most cases).

Different values of minimal p_T 's for the photon and the jet have to be chosen in order to avoid the otherwise present infrared sensitivity of the NLO predictions [11]. This point will be studied in detail later. For inclusive photon cross sections, i.e. in the case where we do not perform a jet analysis of the hadronic final state, we replace the second of the conditions in (12) by a cut on the sum of transverse energies of all final state partons

$$E_T = \sum_{i=q,\bar{q},g} |p_{T,i}| \geq 6 \text{ GeV}. \quad (13)$$

The PDF's of the proton are taken from [16] (MRST). Recent updates of available PDF parametrizations [17, 18] (MRS99, CTEQ5) do not lead to markedly different results (roughly a 2% (4%) increase of the total cross section for MRS99 (CTEQ5) with respect to MRST; a version with enhanced d/u ratio of MRS99 does not lead to observable differences in the range of x and Q^2 considered here). α_s is calculated from the two-loop formula with the same Λ -value ($\Lambda_{\overline{MS}}(n_f = 4) = 300 \text{ MeV}$) as used in the MRST parametrization of the proton PDF. The scale in α_s and the factorization scale are set equal to each other and fixed to the largest $p_{T,J}$, except when we present results with other scale choices. For completeness, we also mention that the slicing cuts have been fixed at $y_0^J = 10^{-4}$ and $y_0^\gamma = 10^{-5}$.

The dependence of the $\gamma +$ jet cross sections on the choice of the photon FF has been studied earlier [12]. In the present work we choose the FF of Bourhis et al. [19] (BFG). This FF has been compared to the ALEPH $e^+e^- \rightarrow \gamma + 1\text{-jet}$ cross section [20] and also to the inclusive photon cross section measured by OPAL [21]. Both data sets agreed well with predictions based on the BFG parametrization [21, 8]. In [12] we studied the cross section differential with respect to the fraction of momentum z_γ carried by a photon inside a jet for several other photon FF's besides the BFG parametrization.

Photon isolation is implemented with the help of the cone isolation method similar to the one used in the ZEUS experiment for photon production with almost real photons

[2]. This method restricts the hadronic energy allowed in a cone around the jet axis of the jet containing the photon. The same method is used also to define jets emerging in the event sample of $\gamma + 2$ -parton-level jets when two partons are combined. In the $\gamma^* p$ center-of-mass frame, two partons i and j are combined into a jet J , when they obey the cone constraints $R_{i,J} < R$ and $R_{j,J} < R$, where

$$R_{i,J} = \sqrt{(\eta_i - \eta_J)^2 + (\phi_i - \phi_J)^2}. \quad (14)$$

η_J ($= -\ln \tan(\theta_J/2)$) and ϕ_J are the rapidity (polar angle θ_J) and azimuthal angle of the recombined jet which are obtained from the formulae

$$\begin{aligned} p_{T,J} &= p_{T,i} + p_{T,j}, \\ \eta_J &= \frac{\eta_i p_{T,i} + \eta_j p_{T,j}}{p_{T,i} + p_{T,j}}, \\ \phi_J &= \frac{\phi_i p_{T,i} + \phi_j p_{T,j}}{p_{T,i} + p_{T,j}}. \end{aligned} \quad (15)$$

For most of the results we choose $R = 1$. If not, we shall state the value of R explicitly. The azimuthal angle is defined with respect to the scattering plane given by the momentum of the beam and the momentum of the scattered electron. The rapidity is always defined positive in the direction of the proton remnant. The photon is treated like any other parton in the recombination process, i.e. when in (14) i or j is the photon, then J is called the photon-jet. To qualify a jet as a photon-jet, we restrict the hadronic energy in the jet by

$$z_\gamma = \frac{p_{T,\gamma}}{p_{T,\gamma} + p_{T,\text{had}}} = 1 - \epsilon_{\text{had}} \geq 1 - \epsilon_{\text{had}}^0 = z_{\text{cut}}. \quad (16)$$

$p_{T,\gamma}$ and $p_{T,\text{had}}$ denote the transverse momenta of the photon and the parton producing hadrons in this jet. Defining $p_{T,\gamma\text{-jet}} = p_{T,\gamma} + p_{T,\text{had}}$, (16) is equivalent to the requirement

$$p_{T,\text{had}} \leq \epsilon_{\text{had}}^0 p_{T,\gamma\text{-jet}}, \quad (17)$$

i.e. the ratio of the total p_T due to other particles (partons) than the photon is required not to exceed ϵ_{had}^0 . For our predictions we shall choose different values for $\epsilon_{\text{had}}^0 = (1 - z_{\text{cut}})$. In [2] this parameter was set equal to $\epsilon_{\text{had}}^0 = 0.11$.

It is known that the cone algorithm is ambiguous for final states with more than three particles or partons [22]. Since we have maximally three partons in the final state this problem is not relevant in our case. However, in some cases it may happen that two partons i and j qualify both as two individual jets i and j , or as a combined jet J . In these exceptional cases we count only the combined jet J to avoid double counting.

The cone algorithm is problematic in experimental analyses due to its seed-finding mechanism and due to overlapping cones. These problems are avoided with the k_T jet finding algorithm [23]. In our theoretical calculations, the k_T algorithm can be incorporated quite

easily: partons i and j (where one of them may be the photon) are combined if they fulfill the condition

$$R_{ij} < R \quad \text{with} \quad R_{ij} = \sqrt{(\eta_i - \eta_j)^2 + (\phi_i - \phi_j)^2}. \quad (18)$$

The resulting kinematic variables of the combined jet are calculated with the same formulae (15) as in the cone algorithm. The recombination condition (14) is equivalent to

$$R_{ij} < Rp_{ij} \quad \text{with} \quad p_{ij} = \frac{p_{T,i} + p_{T,j}}{\max(p_{T,i}, p_{T,j})}. \quad (19)$$

Therefore, choosing the same value for R , jets obtained with the cone algorithm (19) are slightly wider than those constructed with the k_T algorithm (18). In order to demonstrate that our numerical routines work also with the k_T algorithm we have calculated some representative cross sections with this jet definition as well.

3.2 Photon plus Jet Cross Sections

Now we shall present our numerical results. We start with various cross sections for the $\gamma + (n + 1)$ -jet final state since we think that these cross sections, although smaller than the fully inclusive photon cross section, will be measured first due to reduced background problems. It is clear that in NLO the final state may consist of two or three jets where one jet is always a photon jet. The remnant jet is not counted since it is produced with zero transverse momentum. The three-jet sample, equivalent to $\gamma + (2 + 1)$ -jets in the notation of the previous sections, consists of all $\gamma + (2 + 1)$ -parton-level jets which do not fulfill the cone constraint $R_{i,J} < R$ with $R_{i,J}$ given in (14). The $\gamma + (1 + 1)$ -jet sample contains events where two partons (possibly a photon) are recombined into one jet or one parton does not obey the cut on transverse momenta (12). In the following we shall sum over the two samples with $n = 1$ and $n = 2$ jets. If there are two jets in an event, we order them according to their transverse momenta and call the one with larger p_T “jet 1” and the one with smaller p_T accordingly “jet 2”. Also, from now on we will use a simplified notation and denote kinematic variables of the jet containing the photon simply by $p_{T,\gamma}$, η_γ and ϕ_γ .

In Figs. 4 and 5 we show results for the p_T and η dependence of the cross sections $d\sigma/dp_T$ and $d\sigma/d\eta$ for the photon jet and the jet with the largest p_T . In each of the four figures we have plotted three curves for three choices of z_{cut} defined in (16), $z_{\text{cut}} = 0.5, 0.7$ and 0.9 . Together with the cone radius R , z_{cut} controls the amount of photon isolation. As to be expected the cross section decreases with the degree of photon isolation, i.e. with increasing z_{cut} . Specifically in Fig. 4a we present $d\sigma/dp_{T,\gamma}$ as a function of $p_{T,\gamma}$ for the three z_{cut} values and for $p_{T,\gamma} \geq 5$ GeV. All other variables, in particular η_{jet} , η_γ and $p_{T,\text{jet}}$ are integrated over the kinematically allowed ranges. We see that all three cross sections have a similar shape. In Fig. 5a $d\sigma/dp_{T,\text{jet}1}$ as a function of $p_{T,\text{jet}1}$ is shown. The qualitative behaviour of the cross sections for the different z_{cut} ’s is similar as in Fig. 4a.

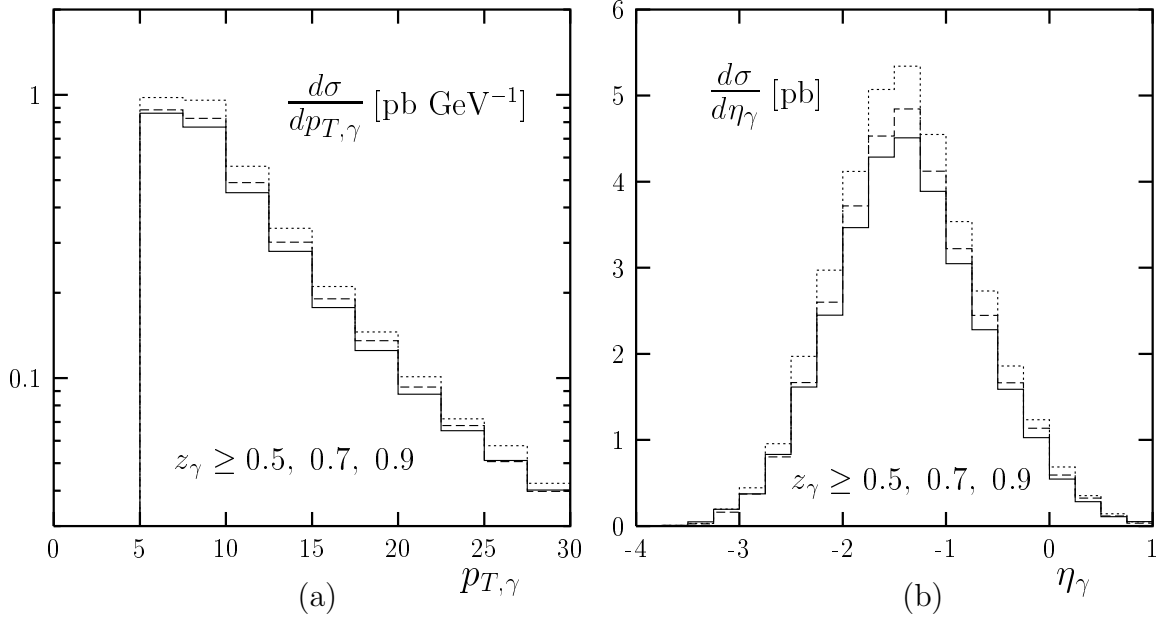


Figure 4: p_T - (a) and η - (b) distributions of the photon jet for $z_{\text{cut}} = 0.9, 0.7$ and 0.5 (full, dashed and dotted curves).

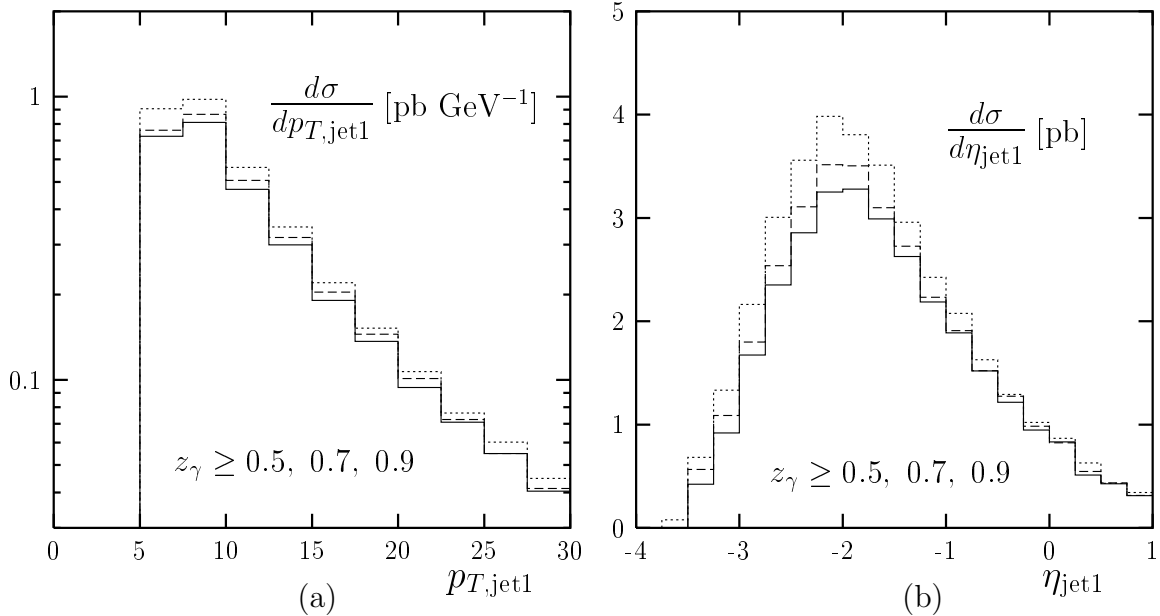


Figure 5: p_T - (a) and η - (b) distributions of the most energetic jet for $z_{\text{cut}} = 0.9, 0.7$ and 0.5 (full, dashed and dotted curves).

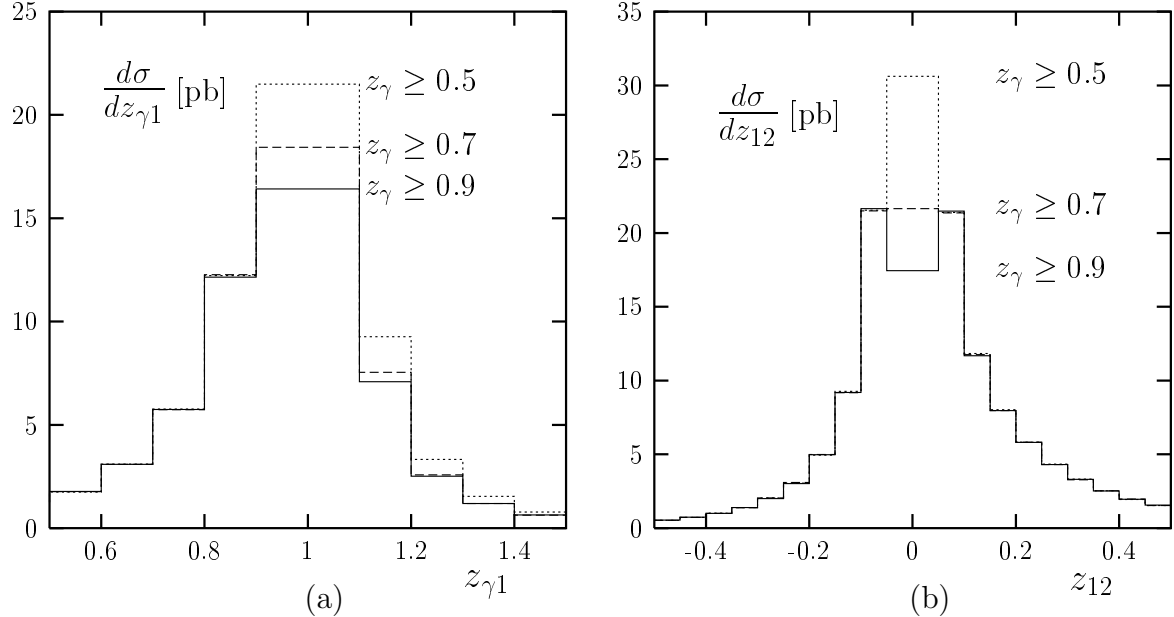


Figure 6: Distribution with respect to the photon-jet imbalance parameter $z_{\gamma 1}$ (a) and the jet-jet imbalance parameter z_{12} (b) for $z_{\text{cut}} = 0.9, 0.7$ and 0.5 (full, dashed and dotted curves).

For the η distributions, shown in Figs. 4b, 5b for the photon jet and the most energetic jet, we have integrated over $p_{T,\gamma} \geq 5$ GeV and $p_{T,\text{jet}1} \geq 6$ GeV. The shapes of the three curves for the different z_{cut} values are similar for both the cross section $d\sigma/d\eta_{\gamma}$ in Fig. 4b and the cross section $d\sigma/d\eta_{\text{jet}1}$ in Fig. 5b. We note that the $\eta_{\text{jet}1}$ distribution peaks at somewhat smaller rapidities than $d\sigma/d\eta_{\gamma}$.

Distributions with respect to p_T and η of the second jet in $\gamma + (2 + 1)$ -jet events do not depend on the isolation cut since in this case each parton (photon) constitutes a jet by its own. Therefore we show corresponding figures in the next subsection when we will discuss the influence of the cone size R on the cross sections.

In addition to predicting distributions in the transverse momenta and the rapidities of the photon and the hadron jets we also have calculated distributions for variables which characterize the correlation of two jets. One of these variables is

$$z_{\gamma 1} = -\frac{\vec{p}_{T,\gamma} \vec{p}_{T,\text{jet}1}}{p_{T,\text{jet}1}^2}. \quad (20)$$

Note that $z_{\gamma 1}$ is defined with the help of the transverse momentum of the photon jet, i.e. $p_{T,\gamma}$ may include a contribution from accompanying hadronic energy. The dependence of the cross section on $z_{\gamma 1}$ characterizes the imbalance in transverse momentum of the photon and the most energetic jet. Similar variables have been used before for studies in the case of photon plus charm jet final states in $p\bar{p}$ collisions [24] and of two-jet production in ep scattering [25]. The result for $d\sigma/dz_{\gamma 1}$ is shown in Fig. 6a for three photon isolation

cuts $z_{\text{cut}} = 0.5, 0.7$ and 0.9 . The cuts on transverse momenta and the cone parameters are as defined before.

For two-body processes such as the LO Compton subprocess $\gamma^* q \rightarrow \gamma q$, the final photon and the jet have balancing transverse momenta and the distribution is a δ -function in $(1 - z_{\gamma 1})$. Also the fragmentation process contributes only to $z_{\gamma 1} = 1$ since in this case the transverse momentum of accompanying hadronic energy is collinear with the photon, resulting in $p_{T,\gamma} = p_{T,\text{bare } \gamma} + p_{T,\text{had}} = p_{T,\text{jet1}}$. Contributions with $z_{\gamma 1} \neq 1$ are due to the higher-order three-body contributions. Events with $z_{\gamma 1} < 1$ typically result from configurations where a single photon is opposite in transverse momentum to a jet consisting of two partons. Since according to the recombination prescription (15) the scalar sum of transverse momenta is ascribed to the jet, not the vectorial sum, one finds always $p_{T,\gamma} < p_{T,\text{jet1}}$ and thus $z_{\gamma 1} < 1$ in this case. Moreover, the photon is never accompanied by a hadronic parton in this case and events with $z_{\gamma 1} < 1$ are consequently not affected by the isolation cut. On the other hand, events with $z_{\gamma 1} > 1$ are predominantly due to configurations with a photon-jet consisting of a photon and a quark or gluon opposite to a jet consisting of a single parton. In this case, a variation of the photon isolation cut z_{cut} has a strong effect on the differential cross section.

These features are clearly visible in Fig. 6a. The cross section increases when lowering z_{cut} , i.e. when larger fragmentation contributions are included. We notice that the $z_{\gamma 1}$ distribution is not symmetric around $z_{\gamma 1} = 1$. The cross section for $z_{\gamma 1} < 1$ is larger than for $z_{\gamma 1} > 1$, becoming more and more symmetric for less restrictive isolation cuts on z_{γ} . The residual asymmetric behaviour of this distribution for vanishing isolation cut is a dynamical property of the underlying cross section.

In the region of $z_{\gamma 1}$ near unity, one of the two final state partons of three-body contributions (not the photon) becomes soft and thus this region is sensitive to soft-gluon effects. In our calculation with an invariant mass cut slicing parameter y_0^J these soft-gluon corrections are considered as two-body contributions. Their contribution depends on the slicing parameter y_0^J . To remove this dependence, i.e. to remove the infrared sensitivity, we must include a sufficiently large fraction of the three-body contribution from outside $z_{\gamma 1} = 1$. Therefore we averaged the $z_{\gamma 1}$ distribution over sufficiently large bins and studied the sum of the $\gamma + (1+1)$ - and $\gamma + (2+1)$ -jet cross sections $d\sigma/dz_{\gamma 1}$. We have chosen a bin width of $\Delta z_{\gamma 1} = 0.2$ around $z_{\gamma 1} = 1$ and $\Delta z_{\gamma 1} = 0.1$ elsewhere.

It is clear that the cross section outside the bin at $z_{\gamma 1} = 1$ has a stronger scale dependence than inside this bin since only three-parton terms contribute. The cross section inside the bin at $z_{\gamma 1} = 1$ is a genuine NLO prediction with expected reduced scale dependence. The scale dependence will be studied later for some other distributions. The δ -function behaviour at LO is of course in reality modified not only by NLO corrections, but also by non-perturbative effects originating from hadronization and a possible intrinsic transverse momentum of the initial parton. Our calculation does not include these latter effects.

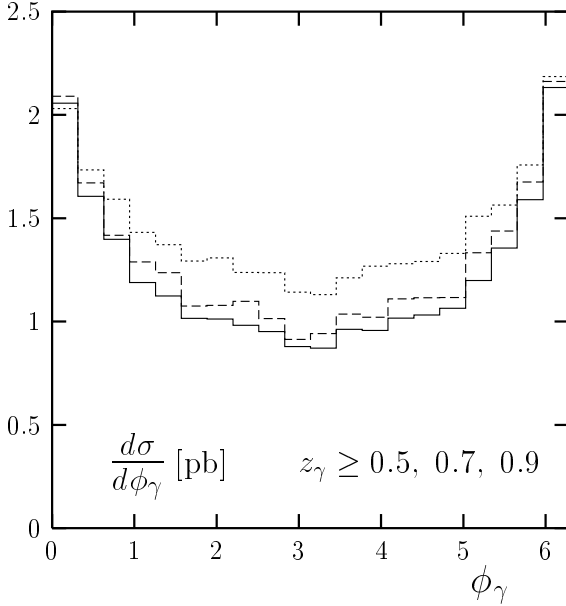


Figure 7: ϕ -distribution of the photon jet for $z_{\text{cut}} = 0.9, 0.7$ and 0.5 (full, dashed and dotted curves).

In Fig. 6b we show the cross section $d\sigma/dz_{12}$ where the variable

$$z_{12} = -\frac{\vec{p}_{T,\text{jet}1}\vec{p}_{T,\text{jet}2}}{p_{T,\text{jet}1}^2} \quad (21)$$

with $p_{T,\text{jet}1} > p_{T,\text{jet}2}$ measures the correlation between the two jets in $\gamma + (2 + 1)$ -jet events. This cross section peaks at $z_{12} = 0$ as to be expected and decreases away from $z_{12} = 0$. The point $z_{12} = 0$ is the point with no second jet, i.e. the pure $\gamma + (1 + 1)$ -jet region. This region is again infrared sensitive. Therefore we integrated here over the bin $-0.05 < z_{12} < 0.05$. Outside this region we chose a bin size of $\Delta z_{12} = 0.05$. Note that the distribution shown in Fig. 6b includes the contribution from low- p_T partons with p_T below the cut in (12). We have also calculated the z_{12} -distribution restricting to $\gamma + (2 + 1)$ -jet events where both jets have $p_T \geq 6$ GeV. In this case, the distribution would extend to larger values of z_{12} with a maximum at $z_{12} \simeq 0.6$. The asymmetric behaviour of the curve visible in Fig. 6b, i.e. the tail at large z_{12} , is due to the contribution from these $\gamma + (2 + 1)$ -jet events.

Another interesting variable might be the azimuthal angle ϕ_γ of the emitted photon. We define ϕ_γ with respect to the plane spanned by the momenta of the beam and of the scattered lepton. In Fig. 7 we show the dependence of the cross section on ϕ_γ , again for the three z_{cut} values $0.5, 0.7$ and 0.9 . As is seen in this figure, the photon is emitted dominantly at $\phi_\gamma = 0$. We note that the distribution becomes flatter with decreasing z_{cut} . It is symmetric within the statistical accuracy of the calculation. We do not present here a similar plot for $d\sigma/d\phi_{\text{jet}1}$, the cross section with respect of the azimuthal angle of the most energetic jet. It would show a distribution which peaks at $\phi_{\text{jet}1} = \pi$, since the dominant contribution to the cross section comes from configurations in which the

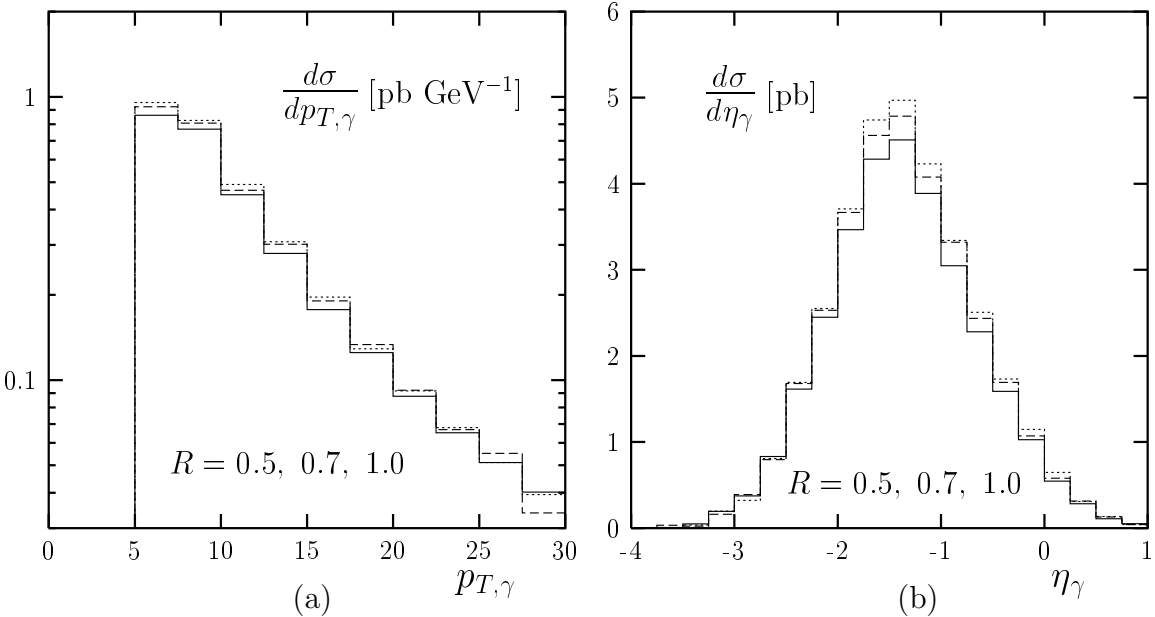


Figure 8: p_T - (a) and η - (b) distributions of the photon jet for $R = 1.0, 0.7$ and 0.5 (full, dashed and dotted curves).

photon and the jet with the largest p_T are emitted back-to-back. For jet 2 there is no such correlation. The cross section $d\sigma/d\phi_{\text{jet}2}$ is independent of $\phi_{\text{jet}2}$ and, in NLO, does not change with z_{cut} . In a similar way one can discuss the cross section as a function of $\phi_{\gamma 1} = \phi_\gamma - \phi_{\text{jet}1}$ or $\phi_{\gamma 2} = \phi_\gamma - \phi_{\text{jet}2}$. $d\sigma/d\phi_{\gamma 1}$ is strongly peaking at $\phi_{\gamma 1} = \pi$. Here it is again necessary to calculate $d\sigma/d\phi_{\gamma 1}$ with a sufficiently large bin size around $\phi_{\gamma 1} = \pi$ in order to avoid any infrared sensitivity. On the other hand, the distribution $d\sigma/d\phi_{\gamma 2}$ is flat around $\phi_{\gamma 2} = 0$ and decreases towards $\phi_{\gamma 2} = \pi$.

3.3 Cone Size Dependence of Jet Cross Sections

So far we presented results only for the cone jet algorithm with the cone radius fixed to $R = 1$ for both the photon jet and purely hadronic jets. Sometimes it is advantageous to use smaller cone radii to suppress background processes. On the other hand the dependence of the cross sections on the cone radius is a genuine NLO effect since LO cross sections do not depend on the jet definition. To present an overview of the cone radius dependence we have recalculated some of the cross sections shown so far for $R = 1$ for two smaller radii $R = 0.5$ and 0.7 . For the photon isolation parameter we fix now $z_{\text{cut}} = 0.9$.

In Figs. 8a, b we show the results for $d\sigma/dp_{T,\gamma}$ and $d\sigma/d\eta_\gamma$ with $R = 0.5, 0.7$, and 1.0 . All other cuts are chosen as before. The case with $R = 1$ and $z_{\text{cut}} = 0.9$ was shown in Figs. 4a, b already. The distributions for the jet with largest p_T are exhibited in Figs. 9a and b. $d\sigma/dp_{T,\gamma}$, $d\sigma/d\eta_\gamma$, $d\sigma/dp_{T,\text{jet}1}$ and $d\sigma/d\eta_{\text{jet}1}$ show very little dependence on the cone

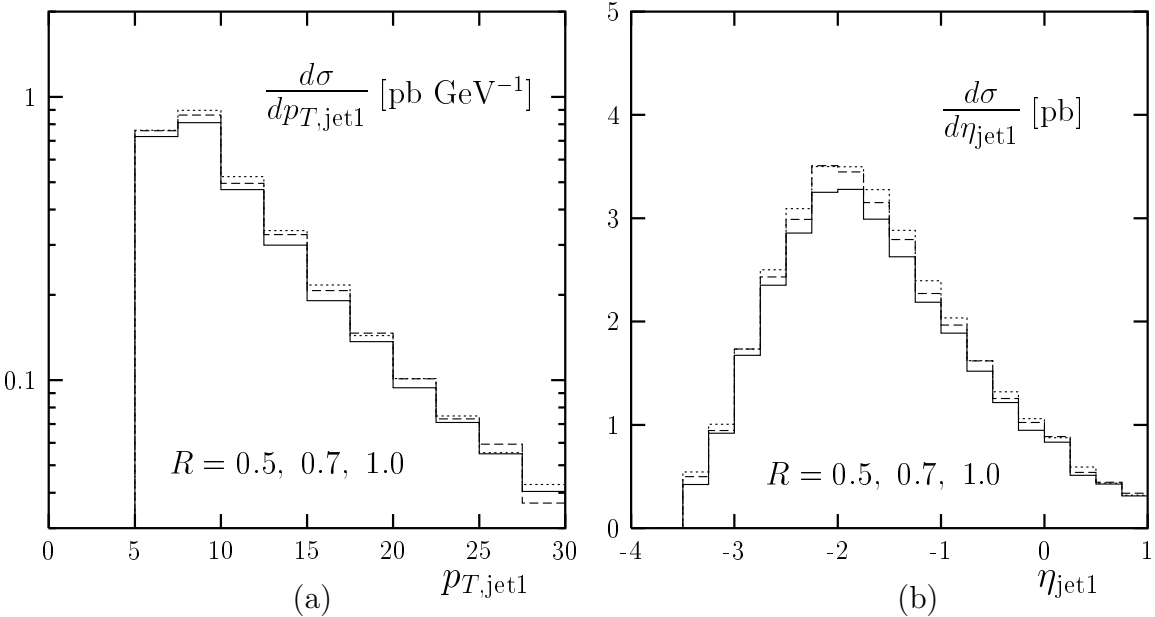


Figure 9: p_T - (a) and η - (b) distributions of the most energetic jet for $R = 1.0, 0.7$ and 0.5 (full, dashed and dotted curves).

size R . For a less restrictive isolation cut of $z_\gamma \geq 0.5$ these distributions would decrease with decreasing cone radius R as it is known from other jet calculations.

In our previous work [11] we studied the equivalent cross sections also for the two event classes with $\gamma + (1+1)$ -jets and $\gamma + (2+1)$ -jets separately. It turned out that the contribution for $\gamma + (1+1)$ -jets is the dominant one. This is expected, since the contribution with $\gamma + (2+1)$ -jets is an $O(\alpha_s)$ effect. Here we present now also results for the p_T and η distributions of jet 2 in this latter process. The results are shown in Fig. 10a ($d\sigma/dp_{T,\text{jet2}}$) and Fig. 10b ($d\sigma/d\eta_{\text{jet2}}$). For $p_{T,\text{jet2}} \geq 6$ GeV the cross section is very much reduced as compared to the cross section in Fig. 9a. In fact, the dominating event configuration is with a photon and one jet balancing each other in p_T ; a third jet with comparable p_T is found in only a small portion of the events. The rapidity distribution $d\sigma/d\eta_{\text{jet2}}$ plotted in Fig. 10b has a larger tail extending to larger rapidities as compared to the cross sections $d\sigma/d\eta_\gamma$ and $d\sigma/d\eta_{\text{jet1}}$. The second energetic jet originates dominantly from the incoming quark and therefore is in many cases closer to the proton remnant, i.e. at positive rapidities, than the harder jet.

The cross sections $d\sigma/dp_{T,\text{jet2}}$ and $d\sigma/d\eta_{\text{jet2}}$ increase with decreasing R . This is the behaviour expected for cross sections which are of leading order in α_s .

In our previous work [12] we studied $d\sigma/dz_\gamma$ as a function of the fraction z_γ of the momentum of the photon inside the photon jet. This cross section is expected to contain information on the photon fragmentation functions. The results presented in [12] were obtained for the case $R = 1$ only. To see how results change with R , we show in Fig. 11 $d\sigma/z_\gamma$ for the particular photon fragmentation function of Bourhis et al. [19] for $R = 0.5$,

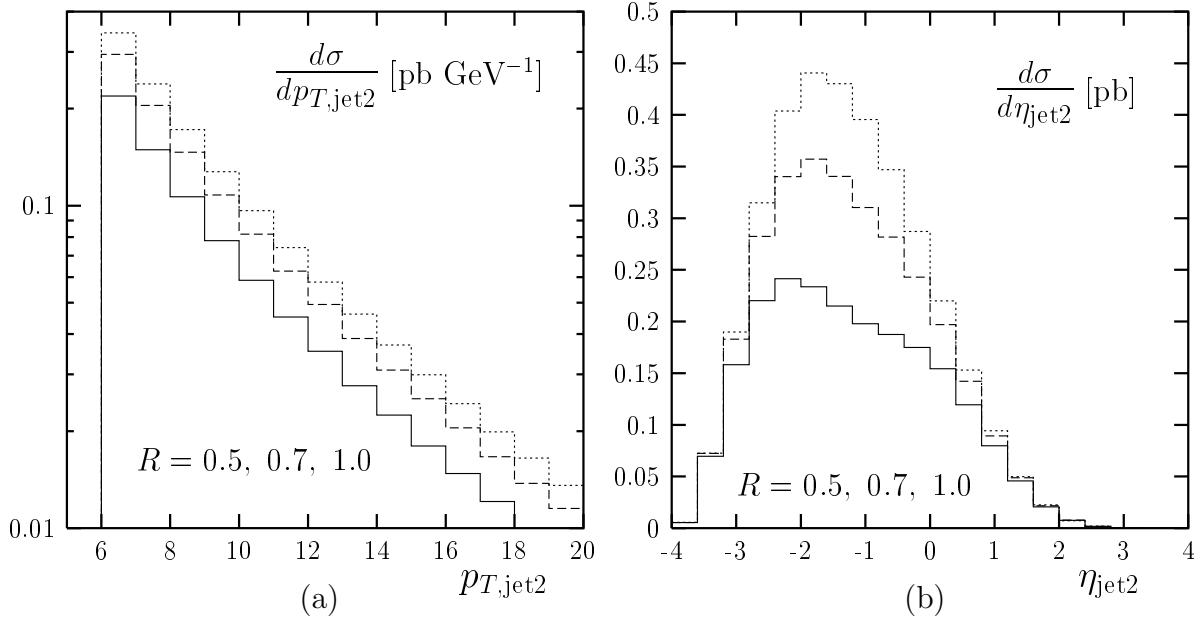


Figure 10: p_T (a) and η (b) distributions of the second, less energetic jet for $R = 1.0, 0.7$ and 0.5 (full, dashed and dotted curves).

0.7 and 1.0. As is seen, $d\sigma/dz_\gamma$ decreases with decreasing R since this cross section is a superposition of leading and next-to-leading order contributions.

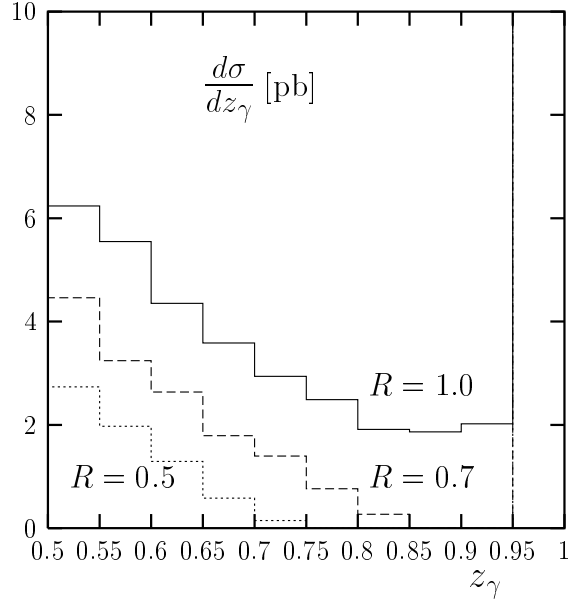


Figure 11: z_γ distributions for $R = 1.0, 0.7$ and 0.5 (full, dashed and dotted curves).

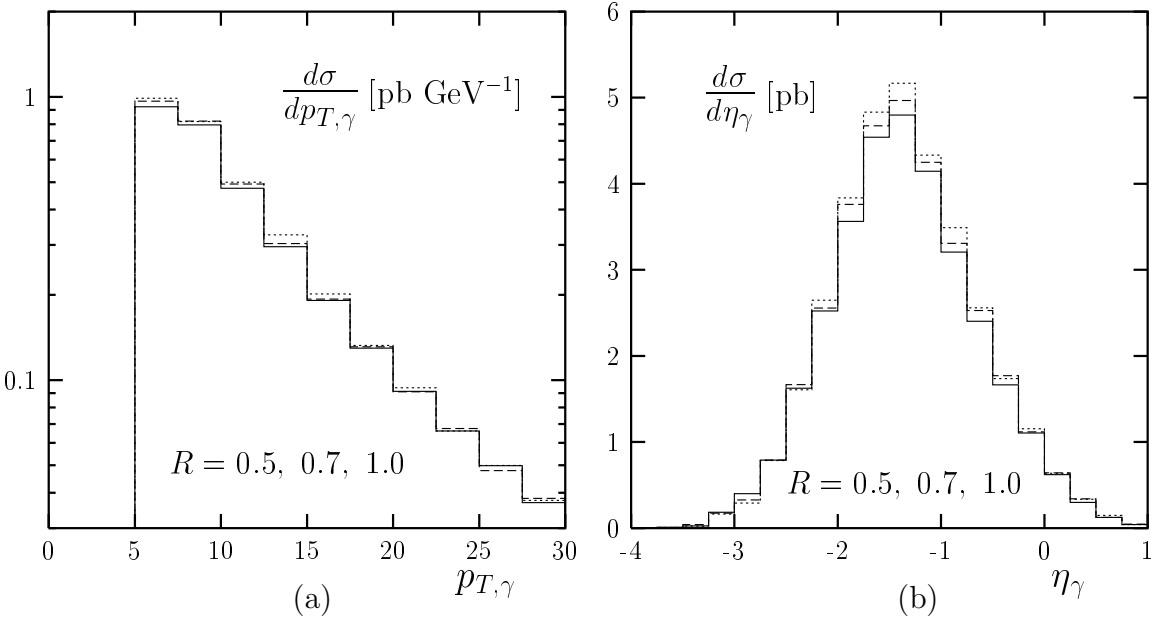


Figure 12: p_T - (a) and η - (b) distributions of the photon jet for $R = 1.0, 0.7$ and 0.5 (full, dashed and dotted curves) in the k_T algorithm.

The R dependence of the other cross sections considered above follows the same pattern. In cases where we have a superposition of LO and NLO contributions we encounter a decreasing cross section with decreasing R . In regions where the cross section receives contribution from $O(\alpha_s)$ only with no additional NLO corrections included, the cross section increases with decreasing R . Thus for example $d\sigma/dz_{\gamma 1}$ (cf. Fig. 6a) is decreasing with R in the bin at $z_{\gamma 1} = 1$ and increasing with R outside this bin, i.e. for $z_{\gamma 1} < 0.9$ and $z_{\gamma 1} > 1.1$. The R dependence of $d\sigma/dz_{12}$ (cf. Fig. 6b) is similar: inside the bin around $z_{12} = 0$ the cross section decreases with decreasing R and outside $z_{12} = 0$ it increases with decreasing R .

3.4 Jet Algorithm Dependence

Measurements of cross sections for the production of a photon plus jets, as for example in γp collisions [2], have been performed with the help of the cone algorithm used to define jets and the photon isolation. However, the k_T algorithm has definite advantages, in particular in the experimental analysis [22]. Therefore we present a few distributions based on the k_T algorithm as well. This algorithm is used for the recombination of two partons into a jet as explained in sect. 3.1 as well as for the definition of the photon jet. In Figs. 12a, 13a we show $d\sigma/dp_{T,\gamma}$ and $d\sigma/dp_{T,\text{jet}1}$ calculated with the k_T algorithm for $R = 0.5, 0.7$ and 1 . These two groups of curves have to be compared to the results with the cone algorithm in Figs. 8a, 9a. The qualitative behaviour of the two cross sections is similar; but there are quantitative differences. We note that the dependence on the

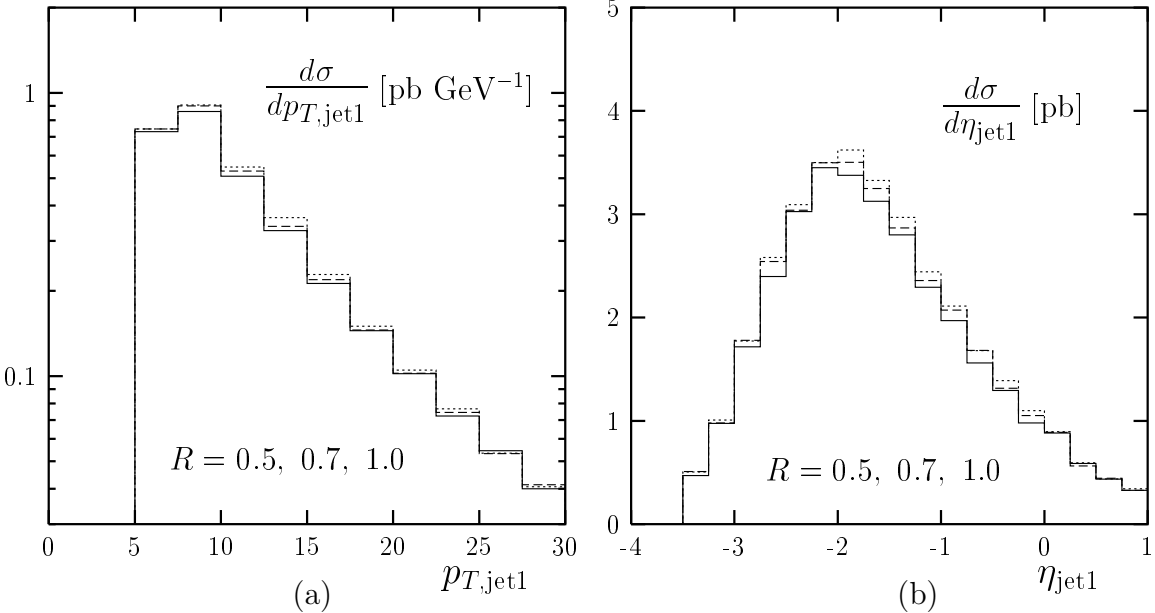


Figure 13: p_T - (a) and η - (b) distributions of the most energetic jet for $R = 1.0, 0.7$ and 0.5 (full, dashed and dotted curves) in the k_T algorithm.

parameter R , which controls the size of the jets, is now even more reduced as compared to the corresponding cross sections with the cone algorithm. The cross sections $d\sigma/d\eta_\gamma$ and $d\sigma/d\eta_{jet1}$ for the k_T algorithm are displayed in Figs. 12b, 13b. They can be compared with the corresponding cross section for the cone algorithm in Figs. 8b, 9b. Similar to the p_T distributions the qualitative behaviour did not change. Again the R dependence seems to be reduced for the k_T algorithm. This is even more the case for the cross sections $d\sigma/dp_{T,jet2}$ and $d\sigma/d\eta_{jet2}$, shown in Figs. 14a, b which should be compared to the corresponding results in Figs. 10a, b. It is clear that the cross sections in Figs. 14a, b increase with decreasing R in the same way as the cross sections for the cone algorithm in Figs. 10a, b.

A direct comparison of cross sections calculated with either the cone algorithm or the k_T algorithm is shown in Fig. 15 (dashed and dotted curves). Here we have chosen $R = 1$ and $z_{cut} = 0.9$. In Figs. 15a, b the cross sections $d\sigma/dp_{T,\gamma}$ and $d\sigma/d\eta_\gamma$ are plotted, respectively. As we can see, these cross sections hardly change when the cone algorithm is replaced by the k_T algorithm. Only where $d\sigma/d\eta_\gamma$ is maximal, i.e. near $\eta_\gamma = -1.5$, the cross section with the k_T algorithm is approximately 5 % larger than with the cone algorithm.

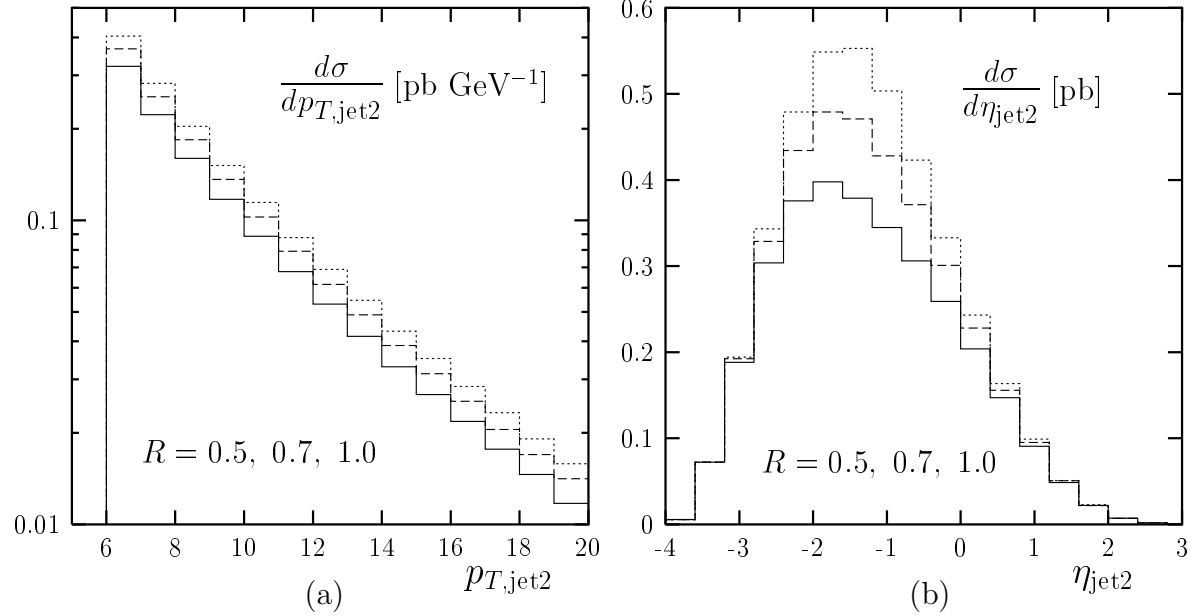


Figure 14: p_T - (a) and η -distributions (b) of the second jet for $R = 1.0, 0.7$ and 0.5 (full, dashed and dotted curves) in the k_T algorithm.

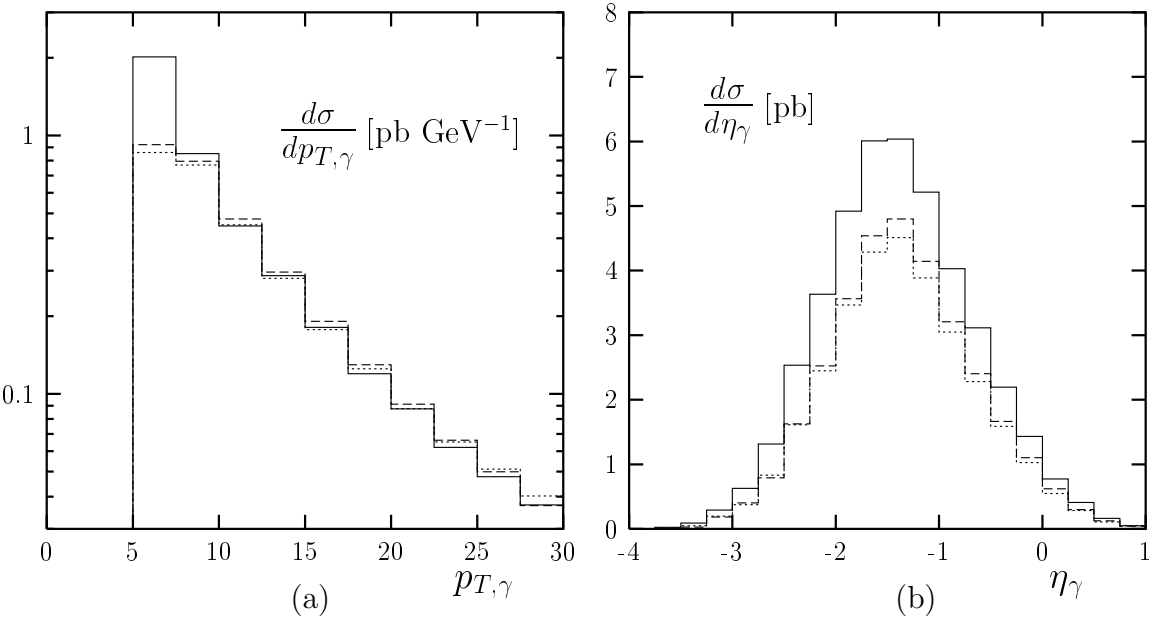


Figure 15: Comparison of the p_T - (a) and η -distributions (b) of the photon jet in the cone algorithm with $z_\gamma \geq 0.9$ and $R = 1.0$ (dotted curves), in the k_T algorithm with $R = 1.0$ (dashed curves) and without jet analysis (inclusive cross section, full curves).

It is expected that the requirement to observe additional jets reduces the cross section for the production of a high- p_T photon. To study this reduction we have calculated also $d\sigma/dp_{T,\gamma}$ and $d\sigma/d\eta_\gamma$ for the inclusive case, i.e. without additional jets required in the final state and the same photon isolation constraint in terms of an isolation cone around the photon and the cut $z_{\text{cut}} = 0.9$. The results for these inclusive cross sections are shown in Figs. 15a, b as full curves. The total cross section without jet algorithm applied is increased by about 35 %. This is reflected in the inclusive cross section $d\sigma/d\eta_\gamma$ which is always larger than the corresponding distribution for final states which are required to contain at least one jet, over the full range of η_γ . In $d\sigma/dp_{T,\gamma}$ only the first two p_T -bins contain an appreciably larger cross section due to the removal of the jet requirement. This can be traced back to the different prescriptions used to remove events with small transverse momentum: for the analyses based on the cone or the k_T jet algorithms, we used the p_T cuts (12) which are applied to individual jets, whereas in the case without jet algorithm we applied the cut (13) to the sum of transverse momenta of all hadronic particles in the final state. As a consequence, an event with two low- p_T partons, each with $p_T < 6$ GeV will be rejected in the first case if these two partons are not recombined into one jet, while the event will be accepted in the second case if the sum of the transverse momenta of the two partons is larger than the cut of 6 GeV. This clearly affects only the bins with lowest p_T .

3.5 Scale Dependence of Jet Cross Sections

All results presented so far have been obtained for a renormalization and factorization scale μ fixed at $\mu = p_{T,\text{jet}1}$ ($\mu = E_T$ of (13) for inclusive cross sections). In LO cross sections, the scale dependence is exclusively due to variations of μ in the parton distribution functions. At NLO we expect that additional terms containing an explicit μ -dependence will reduce the scale dependence. Instead of studying the scale dependence of all the differential cross sections discussed so far separately, we have investigated the scale dependence of some components of the total cross section, i.e. integrated over the phase space allowed by the transverse momentum cuts (12). We define the scale in the form $\mu^2 = f^2 p_{T,\text{jet}1}^2$ and vary f between $f = 1/4$ and 4.

In Fig. 16a we have plotted the f dependence of the $\gamma + (1 + 1)$ -jet cross section in LO and NLO (denoted $O(\alpha_s)$) and of the $\gamma + (2 + 1)$ -jet cross section. The LO cross section (denoted ‘‘Born’’ in Fig. 16) increases with f by approximately 10 % in the range $0.25 < f < 4$. The cross section including corrections of $O(\alpha_s)$ is almost independent of f , i.e. no scale dependence inside the considered range of scales is visible. Here the decrease of the cross section due to the decrease of α_s with increasing f is compensated by the increase originating from the scale dependence of the proton PDF’s. The cross section for the $\gamma + (2 + 1)$ -jet final state, being of order $O(\alpha_s)$, decreases with increasing f by approximately 25 %. This is a combined effect of the dependence of α_s and of the f dependence of the parton distribution functions. The f dependence of separate components (‘‘real’’, ‘‘sing’’ and ‘‘frag’’) of the $\gamma + (1 + 1)$ -jet cross section including $O(\alpha_s)$ terms is plotted in Fig.

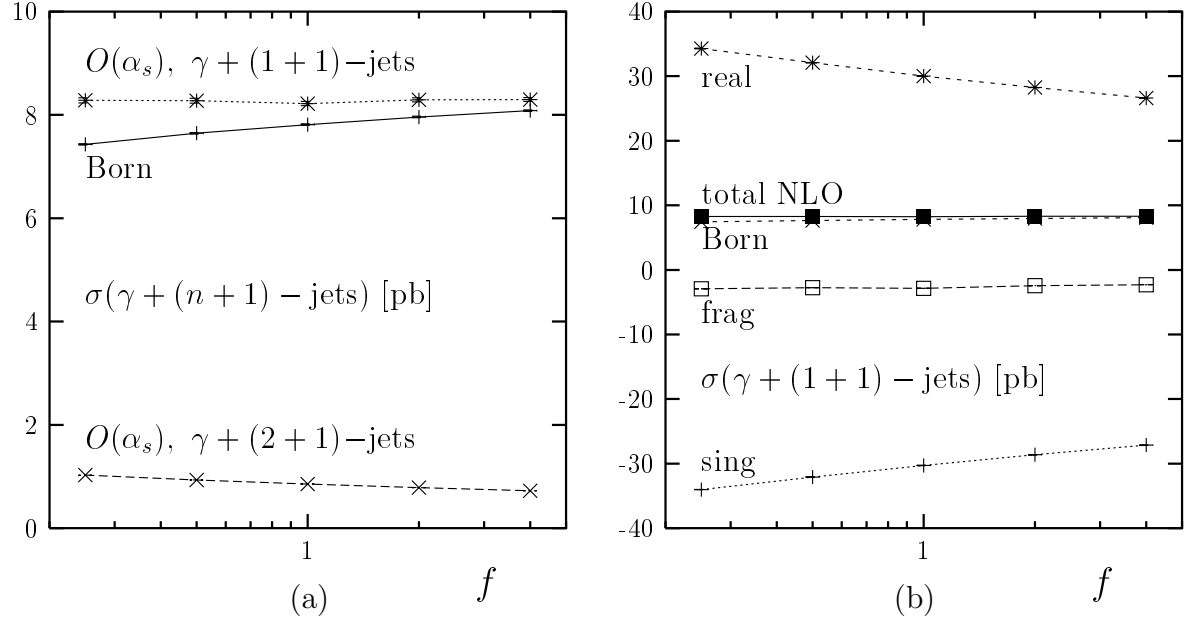


Figure 16: Scale dependence of the total cross section (a) and of separate contributions to the $\gamma + (1+1)$ -jet cross section (b).

16b and again compared with the LO cross section. ‘‘real’’ stands for the tree graph contributions in $O(\alpha_s)$, calculated with the slicing parameter as described in section 2.4. Since it is a tree-graph term it decreases with increasing f due to the decrease of α_s . The singular term ‘‘sing’’, which includes virtual corrections and singular contributions below the slicing cut, is negative and decreases in absolute value by the same amount as ‘‘real’’. The fragmentation contribution ‘‘frag’’ which includes both terms of the right-hand side of (7) is also negative and almost independent of f as expected, since the factorization scale dependence (μ_F in (7)) cancels in first approximation.

3.6 Dependence on Low- p_T Cuts

The choice of two different cuts for the transverse momentum of the photon and the jet is needed to avoid the otherwise present infrared sensitivity of the NLO predictions. This sensitivity is known from similar calculations of dijet cross sections in ep collisions [25] and must be avoided. The same problem was encountered in the calculation of inclusive two-jet cross sections in γp collisions [26], for the production of a prompt photon plus a charm quark in $p\bar{p}$ collisions [24] and much earlier in NLO calculations of the inclusive cross section for photon-hadron [3] and for two-photon production [27].

Above we have chosen the difference between the two $p_{T,\text{min}}$ cuts for the photon and the jet, $\Delta = p_{T,J}^{\text{min}} - p_{T,\gamma}^{\text{min}}$, equal to 1 GeV (see (12)). Δ should not be too small since then we would encounter the infrared sensitive region where the prediction of the cross section becomes unreliable. In order to obtain some information about possible choices for Δ we

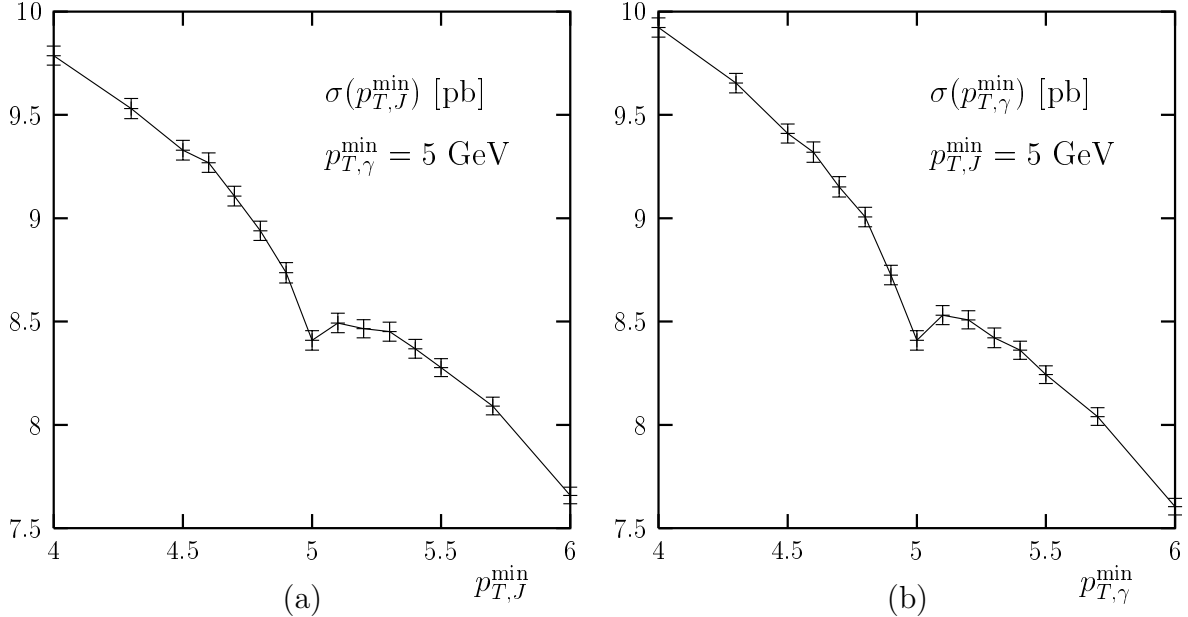


Figure 17: Dependence of the total cross section on lower transverse momentum cutoffs: as a function of $p_{T,J}^{\min}$ with fixed $p_{T,\gamma}^{\min} = 5$ GeV (a) and as a function of $p_{T,\gamma}^{\min}$ with fixed $p_{T,J}^{\min} = 5$ GeV (b).

have studied the $\gamma + (n + 1)$ -jet cross section $d\sigma/dp_{T,J}$ integrated over $p_{T,J} \geq p_{T,J}^{\min}$ as a function of $p_{T,J}^{\min}$. The transverse momentum of the photon was always integrated over the range $p_{T,\gamma} \geq p_{T,\gamma}^{\min} = 5$ GeV. The results for $\sigma(p_{T,J}^{\min})$ are plotted in Fig. 17a. Starting at $p_{T,J}^{\min} = 6$ GeV this cross section increases with decreasing $p_{T,J}^{\min}$ with almost constant slope. At about $p_{T,J}^{\min} = 5.5$ GeV the slope decreases and approaches zero and even changes sign so that $\sigma(p_{T,J}^{\min})$ develops a maximum below $p_{T,J}^{\min} = 5.5$ GeV. This change of slope is due to the infrared sensitivity in the point $p_{T,J}^{\min} = p_{T,\gamma}^{\min}$. To avoid this region one must choose $\Delta \neq 0$. From the plot we observe that $\Delta \geq 0.5$ GeV would be sufficient. Thus, in principle, we could have used a smaller value for this difference than was chosen in (12).

The cross section in the vicinity of $p_{T,J}^{\min} = p_{T,\gamma}^{\min}$ cannot be predicted reliably. It depends on the technical cut y_0^J as soon as one approaches the limit $\Delta = 0$. In fact, the infrared sensitive region is very much influenced by non-perturbative effects which are not included in our calculation. In any case it would be interesting to measure $\sigma(p_T^{\min})$ in order to investigate this non-perturbative region.

In Fig. 17a we present $\sigma(p_{T,J}^{\min})$ also for $p_{T,J}^{\min}$ below 5 GeV, i.e. for $\Delta < 0$. If $p_{T,J}^{\min}$ is increased starting from $p_{T,J}^{\min} = 4$ GeV, the slope of $\sigma(p_{T,J}^{\min})$ changes at about $p_{T,J}^{\min} = 4.5$ GeV and $\sigma(p_{T,J}^{\min})$ becomes smaller towards $p_{T,J}^{\min} = 5$ GeV compared to the behaviour with constant slope. This stronger decrease of $\sigma(p_{T,J}^{\min})$ above $p_{T,J}^{\min} = 4.5$ has its origin again in the infrared sensitivity of this region. For $p_{T,J}^{\min} \rightarrow 5$ GeV, and $\Delta < 0$ the cross section approaches the same value as we have obtained for $\Delta \rightarrow 0$ in the region $\Delta > 0$. This means, $\sigma(p_{T,J}^{\min})$ is not singular at $p_{T,J}^{\min} = 5$ GeV, nor has it a discontinuity.

The observed behaviour is of course not only visible at the specific value of $p_T^{\min} = 5$ GeV which we have chosen. A similar dip is seen for larger and smaller values as well. It becomes more pronounced for smaller values and gets washed out for larger p_T^{\min} .

For completeness we show in Fig. 17b also the cross section with the roles of $p_{T,J}^{\min}$ and $p_{T,\gamma}^{\min}$ interchanged, i.e. we fix $p_{T,J}^{\min} = 5$ GeV and study the dependence on the cut for the photon transverse momentum $p_{T,\gamma}^{\min}$. The behaviour of the cross section in Fig. 17b is very similar to the first case and shows the same infrared sensitive region. Inside the region $-0.5 \text{ GeV} < \Delta < 0.5 \text{ GeV}$ the cross sections agree inside numerical errors. Only for larger $|\Delta|$ the dependences on the minimal transverse momenta of the jet and the photon become different. The cross sections shown in Fig. 17 have been calculated with the cone algorithm using $R = 1$ and $z_{\text{cut}} = 0.9$.

4 Summary and Concluding Remarks

We have presented results of a next-to-leading order calculation of isolated photon production in large- Q^2 ep scattering. Contributions from quark-to-photon fragmentation are explicitly taken into account. We have discussed numerical results for $\gamma + (1+1)$ -jet and $\gamma + (2+1)$ -jet cross sections as functions of transverse momenta, rapidity and other observables derived from photon and/or jet kinematic variables. Infrared sensitive regions, as for example the region of equal photon and jet p_T , are studied in detail.

We investigated several of these cross sections with respect to their photon isolation, jet cone size, scale and jet algorithm dependences. It was found that these dependences are rather weak. In particular, the scale dependence of the integrated cross section is very small, giving quite some confidence in the reliability of our predictions. Also the results depended very little on the choice of modern parton distribution functions for the proton.

We expect that the measurement of photon plus jet cross sections at HERA will contribute to testing perturbative QCD in the process $\gamma^* p \rightarrow \gamma X$, in an area which has not been studied yet. The calculation covers the range of large Q^2 where the results do not depend on parton distribution functions of the virtual photon. At even larger Q^2 additional contributions from Z boson exchange become important, which have been neglected in the present calculation. It is no major problem to incorporate these missing parts. They are non-negligible and must be considered when experimental data become available at very large Q^2 .

References

[1] For a recent discussion see: L. Apanasevich et al., Phys. Rev. **D59** (1999) 074007, and the earlier references given there.

- [2] J. Breitweg et al., ZEUS Collaboration, Phys. Lett. **B413** (1997) 201; K. Müller, Proceedings of the Eur. Phys. Soc. *High Energy Physics Conference*, Jerusalem 1997, p. 464; J. Breitweg et al., ZEUS Collaboration, DESY-99-161, October 1999, (to appear in Phys. Lett. B).
- [3] P. Aurenche, R. Baier, A. Douiri, M. Fontannaz and D. Schiff, Z. Phys. **C24** (1984) 309.
- [4] K. Koller, T. F. Walsh and P. M. Zerwas, Z. Phys. **C2** (1979) 197.
- [5] H. Baer, J. Ohnemus and F. F. Owens, Phys. Rev. **D41** (1990) 61; P. Aurenche et al., Nucl. Phys. **B399** (1993) 34; L. E. Gordon and W. Vogelsang, Phys. Rev. **D50** (1994) 1901; L. E. Gordon, E. Reya and W. Vogelsang, Phys. Rev. Lett. **73** (1994) 388.
- [6] G. Kramer and B. Lampe, Phys. Lett. **B269** (1991) 401; G. Kramer and H. Spiesberger, Proceedings *Workshop on Photon Radiation from Quarks*, Annecy 1991, CERN Yellow Report 92-04, p. 26; E. W. N. Glover and W. J. Stirling, Phys. Lett. **B295** (1992) 128; Z. Kunszt and Z. Trócsányi, Nucl. Phys. **B394** (1993) 139; E. L. Berger, X. Guo and J. Qiu, Phys. Rev. **D54** (1996) 5470.
- [7] A. Gehrman-De Ridder, T. Gehrman and E. W. N. Glover, Phys. Lett. **B414** (1997) 354.
- [8] A. Gehrman-De Ridder and E. W. N. Glover, Nucl. Phys. **B517** (1998) 269; Eur. Phys. J. **C7** (1999) 29.
- [9] P. Aurenche et al., Z. Phys. **C56** (1993) 589; L. E. Gordon and J. K. Storrow, Z. Phys. **C63** (1994) 581; L. E. Gordon and W. Vogelsang, Phys. Rev. **D52** (1995) 58; L. E. Gordon, Phys. Rev. **D57** (1998) 235; M. Krawczyk and A. Zembrzuski, Proceedings of the *29th International Conference on High-Energy Physics (ICHEP 98)*, Vancouver, Canada, 23-29 July 1998, Vol. 1, p. 895, (hep-ph/9810253).
- [10] G. Kramer, D. Michelsen and H. Spiesberger, Eur. Phys. J. **C5** (1998) 293.
- [11] A. Gehrman-De Ridder, G. Kramer and H. Spiesberger, Phys. Lett. **B459** (1999) 271.
- [12] A. Gehrman-De Ridder, G. Kramer and H. Spiesberger, Eur. Phys. J. **C11** (1999) 137.
- [13] D. Michelsen, doctoral thesis, University of Hamburg, 1995, DESY-95-146.
- [14] K. Fabricius, G. Kramer, G. Schierholz and I. Schmidt, Z. Phys. **C11** (1982) 315; F. Gutbrod, G. Kramer and G. Schierholz, Z. Phys. **C21** (1984) 235; W. T. Giele and E. W. N. Glover, Phys. Rev. **D46** (1992) 1980.

- [15] E. W. N. Glover and A. G. Morgan, Z. Phys. **C62** (1994) 311.
- [16] A. D. Martin, R. G. Roberts, W. J. Stirling and R. S. Thorne, Eur. Phys. J. **C4** (1998) 463.
- [17] A. D. Martin, R. G. Roberts, W. J. Stirling and R. S. Thorne, Univ. Durham preprint DTP/99/64 (1999), (hep-ph/9907231).
- [18] H. L. Lai et al., Phys. Rev. **D55** (1997); H. L. Lai and W. K. Tung, Z. Phys. **C74** (1997) 463; H. L. Lai et al., Eur. Phys. J. **C12** (2000) 375.
- [19] L. Bourhis, M. Fontannaz and J. Ph. Guillet, Eur. Phys. J. **C2** (1998) 529.
- [20] D. Buskulic et al., ALEPH Collaboration, Z. Phys. **C69** (1996) 365.
- [21] K. Ackerstaff et al., OPAL Collaboration, Eur. Phys. J. **C2** (1998) 39.
- [22] M. H. Seymour, Nucl. Phys. **B513** (1998) 269.
- [23] S. Catani, Y. L. Dokshitzer, M. H. Seymour and B. R. Webber, Nucl. Phys. **B406** (1993) 187; S. D. Ellis and D. E. Soper, Phys. Rev. **D48** (1993) 3160.
- [24] B. Bailey, E. L. Berger and L. E. Gordon, Phys. Rev. **D54** (1996) 1896; E. L. Berger and L. E. Gordon, Phys. Rev. **D54** (1996) 2279.
- [25] G. Kramer and B. Pötter, Eur. Phys. J. **C5** (1998) 665.
- [26] M. Klasen and G. Kramer, Phys. Lett. **B366** (1996) 385; S. Frixione and G. Ridolfi, Nucl. Phys. **B507** (1997) 315.
- [27] P. Aurenche, A. Douiri, R. Baier, M. Fontannaz and D. Schiff, Z. Phys. **C29** (1985) 459.